

Theoretical synthesis of small-angle neutron scattering spectra with a smearing effect from monodisperse and polydisperse hard spherical colloids

Shuoyang Xiao(肖硕洋), Songlin Wang(王松林), Bin Wu(吴彬), and Takuya Iwashita
Citation: Chin. Phys. B, 2026, 35 (**3**): 036106. DOI: 10.1088/1674-1056/adf61c
http://cpb.iphy.ac.cn; http://iopscience.iop.org/cpb

What follows is a list of articles you may be interested in

Stokes-Einstein-Debye relation in TIP5P water

Gan Ren(任淦)
Chin. Phys. B, 2025, 34 (**2**): 026101. DOI: 10.1088/1674-1056/ad94e3

Structural and thermodynamic properties of inhomogeneous fluids in rectangular corrugated nano-pores

Yanshuang Kang(康艳霜), Haijun Wang(王海军), and Zongli Sun(孙宗利)
Chin. Phys. B, 2022, 31 (**5**): 056104. DOI: 10.1088/1674-1056/ac4237

Small-angle neutron scattering study on the stability of oxide nanoparticles in long-term thermally aged 9Cr-oxide dispersion strengthened steel

Peng-Lin Gao(高朋林), Jian Gong(龚建), Qiang Tian(田强), Gung-Ai Sun(孙光爱), Hai-Yang Yan(闫海洋),Liang Chen(陈良), Liang-Fei Bai(白亮飞), Zhi-Meng Guo(郭志猛), and Xin Ju(巨新)
Chin. Phys. B, 2022, 31 (**5**): 056102. DOI: 10.1088/1674-1056/ac43aa

A revised jump-diffusion and rotation-diffusion model

Hua Li(李华), Yu-Hang Chen(陈昱沆), Bin-Ze Tang(唐宾泽)
Chin. Phys. B, 2019, 28 (**5**): 056105. DOI: 10.1088/1674-1056/28/5/056105

Recent progress on magnetic-field studies on quantum-spin-liquid candidates

Zhen Ma(马祯), Kejing Ran(冉柯静), Jinghui Wang(王靖珲), Song Bao(鲍嵩), Zhengwei Cai(蔡正蔚), Shichao Li(李世超), Jinsheng Wen(温锦生)
Chin. Phys. B, 2018, 27 (**10**): 106101. DOI: 10.1088/1674-1056/27/10/106101

Theoretical synthesis of small-angle neutron scattering spectra with a smearing effect from monodisperse and polydisperse hard spherical colloids

Shuoyang Xiao(肖硕洋)[1], Songlin Wang(王松林)[2,3], Bin Wu(吴彬)[1,†], and Takuya Iwashita[4,‡]

[1] *School of Physics and Astronomy, Beijing Normal University, Beijing* 100875, *China*
[2] *Dongguan Neutron Science Center, Dongguan* 523800, *China*
[3] *Institute of High Energy Physics, Chinese Academy of Sciences, Beijing* 100049, *China*
[4] *Department of Science and Technology, Oita University, Oita* 870-1192, *Japan*

(Received 4 June 2025; revised manuscript received 28 July 2025; accepted manuscript online 31 July 2025)

Small-angle neutron scattering (SANS) is a powerful technique for microstructural characterization with several advantages, such as unique isotopic sensitivity, deep penetration capability, *in situ* characterization potential, and minimal radiation damage to samples. However, the intrinsically low neutron flux unavoidably necessitates certain compromises during measurements. These include a finite spread in wavelength, beam divergence, and the large footprint of the incident neutron beam, all of which lead to the so-called smearing effect. Consequently, the measured SANS spectra not only encode the microstructural information of the samples but are also influenced by the experimental conditions, thereby complicating the interpretation of the data. To facilitate the development of a machine learning-based approach for de-smearing measured SANS spectra, this study aims to establish a theoretical framework for synthesizing spectra both with and without the smearing effect. We focus on hard-sphere colloidal systems and consider system parameters such as the colloidal particle size, polydispersity, and volume fraction, and measurement conditions such as the neutron wavelength and its spread and beam divergence. The exemplary spectra presented herein also highlight the impact of the smearing effect under typical experimental conditions.

Keywords: small-angle neutron scattering, smearing effect, hard-sphere colloidal systems, spectral analysis

PACS: 61.05.fg, 61.20.Gy

DOI: 10.1088/1674-1056/adf61c **CSTR:** 32038.14.CPB.adf61c

1. Introduction

The SANS technique is a powerful tool for characterizing the microstructure of materials. In contrast to x-rays, neutrons interact with atomic nuclei rather than electrons; therefore, the scattering length does not vary systematically with the atomic number; in particular, wide variation in SANS contrast can be readily achieved through isotopic substitution without considerably altering the physicochemical properties of the system being characterized.[1–3] Furthermore, neutrons exhibit strong penetrating power, allowing for *in situ* measurement in complex sample environments.[4,5] Additionally, neutrons with wavelengths suitable for the scattering technique carry relatively low energies, promising minimal radiation damage to samples.[6,7] These advantages render the SANS technique beneficial in the study of soft matter, including colloids,[8–10] polymers,[11–14] latexes,[15,16] and surfactants.[17–19] Nevertheless, the fluxes of neutron sources are typically 5–6 orders of magnitude lower than those of x-ray sources. For example, the photon flux at the BioSAXS beamline (BL19U2) of the Shanghai Synchrotron Radiation Facility (SSRF) reaches the order of 10^{12} photons per second,[20] whereas the neutron flux at the SANS instrument of the China Spallation Neutron Source (CSNS) is approximately 10^7 neutrons per second.[21] As such, to complete measurements within a reasonable time, certain compromises are inevitable. For example, the footprint of the incident neutron beam (on the order of centimeters) is much larger than that of the incident x-ray beam (on the order of micrometers), and the wavelength spread of the incident neutron beam is significantly broader than that of its x-ray counterpart. These compromises increase the uncertainty in determining the momentum transfer of the scattered neutrons and introduce discernible smearing effects.[22–25] In qualitative terms, the experimentally collected SANS spectrum not only contains the diffraction pattern that reflects the sample's microstructure but also includes an additional resolution function that is relevant to the measurement setup;[25,26] this complication makes SANS data analysis difficult.

There have been tremendous efforts devoted to removing the resolution function from experimentally obtained SANS spectra. Herein, we highlight three major approaches. First, the Fourier transform method converts the convolution relationship between the diffraction pattern and resolution func-

†Corresponding author. E-mail: bwu6@bnu.edu.cn
‡Corresponding author. E-mail: tiwashita@oita-u.ac.jp

© 2026 Chinese Physical Society and IOP Publishing Ltd. All rights, including for text and data mining, AI training, and similar technologies, are reserved.

tion in reciprocal space into a product relationship in real space. This transformation facilitates decoupling, leading to the so-called pair distance distribution function (PDDF). Note that PDDF is not to be confused with pair distribution function (PDF). However, direct transformation inevitably suffers from truncation errors due to the limited q-range accessible from experiments, where q (a quantity in reciprocal space) represents the momentum transfer of the scattered neutrons and is converted to distance r in real space via Fourier transform. To overcome this limitation, Glatter *et al.* devised an indirect Fourier transform method in which a set of basis functions[27–29] is employed to reconstruct the PDDF. Nonetheless, in dilute solutions, the derived PDDF provides statistical information about internal distance distributions within an individual particle (e.g., protein) rather than a direct structural representation, making it challenging to understand the structural characteristics. In high-concentration solutions, the PDDF additionally incorporates interparticle correlations, further complicating its interpretation. Second, the model fitting method involves constructing a model of the sample's microstructure, calculating the corresponding theoretical diffraction curve on the basis of assumed parameters, and then convolving it with the instrumental resolution function. The resulting smeared curve is then compared to the actual experimental spectrum. This process is repeated to optimize the model parameters until the best agreement is achieved between the theoretically synthesized and experimentally measured spectra.[26,29,30] While effective in some cases, this approach is difficult to apply to systems involving particles with irregular shapes or complicated interparticle interactions because of challenges in accurately modeling both intra- and interparticle correlations. Third, iterative methods, such as the Lake and Van Cittert algorithms, are also widely used.[31,32] However, these algorithms lack well-defined stopping criteria and tend to perform poorly in the presence of large statistical errors.[33] In addition to the three aforementioned approaches, other approaches are being actively explored.[34]

Recently, machine learning (ML) techniques have demonstrated powerful capabilities in analyzing and processing complex data. In particular, researchers have started applying ML techniques to the analysis of SANS spectra. For example, Tung *et al.* integrated convolutional neural networks (CNNs) with variational autoencoders (VAEs) to recognize structural characteristics in distorted lamellar phases;[35] Song *et al.* employed CNNs to classify two-dimensional (2D) scattering patterns, facilitating the identification of material structures in the early stages of the experiment.[36] In another study, Chang *et al.* applied ML techniques to establish a mapping relationship between low-resolution, short-time measurement spectra and high-resolution, long-time measurement spectra, with the aim of reducing the experimental time.[37] These pioneering efforts naturally motivated the development of an ML-based de-smearing protocol for SANS analysis.

Notably, the performance of ML models depends highly on the availability of large-scale, high-quality training datasets. Such datasets should include paired information consisting of the diffraction curve, resolution function, and smeared SANS spectrum and should encompass a broad range of measurement conditions across various representative sample systems. In this work, the term diffraction curve refers to the ideal SANS spectrum unaffected by the smearing effect, whereas the terms smeared SANS spectrum (also referred to as the measured SANS spectrum) refer to the SANS spectrum that includes the smearing effect. To generate the required training datasets, theoretical synthesis represents the most practical and reliable approach. As our first effort in this direction, we focus on monodisperse and polydisperse hard-sphere colloidal solutions and outline the theoretical framework necessary for dataset generation.

The rest of this paper is organized as follows. In the second part, we provide a concise overview of the theoretical framework and list the associated parameters; in the third part, by systematically adjusting parameters such as the particle diameter, volume fraction, and wavelength of the incident neutron beam, we generate a series of exemplary diffraction curves, resolution functions, and smeared SANS spectra. Our work should facilitate the application of ML techniques in SANS data analysis.

2. Theoretical background

In SANS, the diffraction curves are composed of coherent and incoherent scattering contributions. Because the incoherent contributions are generally considered q-independent and thus do not carry structural information, they are neglected in the following derivations.

2.1. Colloids of spherically identical particles

The following derivation can also be referred from the review paper by Chen.[38] By assuming that the interaction of an incident neutron with a given nucleus is independent of its interactions with other nuclei, the normalized coherent neutron scattering intensity $I_{\mathrm{coh}}(\boldsymbol{q})$ from a colloidal solution can be expressed as follows:

$$I_{\mathrm{coh}}(\boldsymbol{q}) = \frac{1}{V}\left\langle \left| \sum_{k=1}^{N} b_k \, \mathrm{e}^{\,\mathrm{i}\boldsymbol{q}\cdot\boldsymbol{r}_k} \right|^2 \right\rangle, \tag{1}$$

where V is the illuminated volume of the sample exposed to the incident neutrons, b_k represents the coherent bound scattering length for the k-th nucleus, $\boldsymbol{r}_k$ denotes the position vector, $\boldsymbol{q}$ represents the momentum transfer, and i represents the imaginary number. The summation runs over all the nuclei within V, totaling N. The angular bracket $\langle\cdot\rangle$ denotes ensemble averaging.

Since a colloidal system typically consists of two distinct phases, colloidal particles and the surrounding solvent, the summation inside the angular bracket of Eq. (1) can be accordingly divided into two corresponding components, as shown below:

$$I_{\mathrm{coh}}(\boldsymbol{q}) = \frac{1}{V}\left\langle \left| \sum_{k=1}^{N^{\mathrm{C}}} b_k \mathrm{e}^{\mathrm{i}\boldsymbol{q}\cdot\boldsymbol{r}_k} + \sum_{k=1}^{N^{\mathrm{S}}} b_k \mathrm{e}^{\mathrm{i}\boldsymbol{q}\cdot\boldsymbol{r}_k} \right| \right\rangle, \tag{2}$$

where N^{C} and N^{S} are the numbers of nuclei that belong to the colloidal particles and solvents, respectively, within the illuminated volume V.

Next, we proceed to model the first term, which represents the contribution from the colloidal particles. Based on the idea of vector decomposition, the position of an arbitrary k-th nucleus within a given J-th colloidal particle can be expressed as follows:

$$\boldsymbol{r}_k = \boldsymbol{r}_J^k + \boldsymbol{R}_J, \tag{3}$$

where $\boldsymbol{R}_J$ denotes the position vector of the center of the J-th colloidal particle and $\boldsymbol{r}_J^k$ represents the vector pointing from the center of that particle to the position of its k-th nucleus. Hence, the summation over all the nuclei belonging to the colloidal particles can be reformulated as a nested summation, as shown below:

$$\sum_{k=1}^{N^{\mathrm{C}}} b_k \mathrm{e}^{\mathrm{i}\boldsymbol{q}\cdot\boldsymbol{r}_k} = \sum_{J=1}^{N_{\mathrm{p}}} \sum_{k=1}^{N_{\mathrm{n}}} b_k \mathrm{e}^{\mathrm{i}\boldsymbol{q}\cdot\boldsymbol{r}_J^k} \mathrm{e}^{\mathrm{i}\boldsymbol{q}\cdot\boldsymbol{R}_J}, \tag{4}$$

where the outer summation runs over the total number of colloidal particles, denoted N_{p}, while the inner summation runs over the number of nuclei within a single colloidal particle, denoted N_{n}. The total number of nuclei associated with the colloidal particles is given by $N^{\mathrm{C}} = N_{\mathrm{p}} \times N_{\mathrm{n}}$. Note that N_{n} is independent on N_{p}, because colloidal particles are assumed to be identical. Therefore, the two summations can be carried out separately and one obtains the following expression:

$$\sum_{k=1}^{N^{\mathrm{C}}} b_k \mathrm{e}^{\mathrm{i}\boldsymbol{q}\cdot\boldsymbol{r}_k} = \sum_{k=1}^{N_{\mathrm{n}}} b_k \mathrm{e}^{\mathrm{i}\boldsymbol{q}\cdot\boldsymbol{r}_J^k} \times \sum_{J=1}^{N_{\mathrm{P}}} \mathrm{e}^{\mathrm{i}\boldsymbol{q}\cdot\boldsymbol{R}_J}. \tag{5}$$

Next, we introduce the continuum approximation, wherein the distribution of the bound scattering lengths within a colloidal particle is treated as continuous. This yields the concept of the scattering length density, denoted $\rho_{\mathrm{P}}(\boldsymbol{r})$, which represents the accumulated bound scattering length per unit volume at position $\boldsymbol{r}$ inside the volume occupied by the colloidal particle, denoted V_{p}. Hence, equation (5) can be reformatted as follows:

$$\sum_{k=1}^{N^{\mathrm{C}}} b_k \mathrm{e}^{\mathrm{i}\boldsymbol{q}\cdot\boldsymbol{r}_k} = \int_{V_{\mathrm{p}}} \rho_{\mathrm{P}}(\boldsymbol{r}) \mathrm{e}^{\mathrm{i}\boldsymbol{q}\cdot\boldsymbol{r}} \mathrm{d}\boldsymbol{r} \times \sum_{J=1}^{N_{\mathrm{P}}} \mathrm{e}^{\mathrm{i}\boldsymbol{q}\cdot\boldsymbol{R}_J}. \tag{6}$$

The continuum approximation is also applicable to the solvent. Moreover, since the solvent molecules are sufficiently small such that either their internal structure or the correlation among distinct solvent molecules is outside the accessible range of SANS, the scattering length density of the solvent can be effectively approximated as a constant. For example, the scattering length density of H_2O and D_2O water can be calculated as follows:

$$\rho_{\mathrm{H_2O}} = \frac{2b_{\mathrm{H}} + b_{\mathrm{O}}}{V_{\mathrm{H_2O}}} = \frac{2\times(-3.741)\times10^{-13}\ \mathrm{cm} + 5.803\times10^{-13}\ \mathrm{cm}}{2.990\times10^{-23}\ \mathrm{cm}^3} \approx -5.615\times10^{9}\ \mathrm{cm}^{-2}, \tag{7}$$

$$\rho_{\mathrm{D_2O}} = \frac{2b_{\mathrm{D}} + b_{\mathrm{O}}}{V_{\mathrm{D_2O}}} = \frac{2\times6.671\times10^{-13}\ \mathrm{cm} + 5.803\times10^{-13}\ \mathrm{cm}}{2.990\times10^{-23}\ \mathrm{cm}^3} \approx 6.403\times10^{10}\ \mathrm{cm}^{-2}. \tag{8}$$

Let the scattering length density of the solvent be denoted ρ_{s}. Then, the second term of Eq. (2) can be further expressed as

$$\begin{aligned}\sum_{k=1}^{N^{\mathrm{S}}} b_k \mathrm{e}^{\mathrm{i}\boldsymbol{q}\cdot\boldsymbol{r}_k} &= \int_{V} \rho_{\mathrm{s}} \mathrm{e}^{\mathrm{i}\boldsymbol{q}\cdot\boldsymbol{r}} \mathrm{d}\boldsymbol{r} \\ &\quad - \int_{V_{\mathrm{p}}} \rho_{\mathrm{s}} \mathrm{e}^{\mathrm{i}\boldsymbol{q}\cdot\boldsymbol{r}} \mathrm{d}\boldsymbol{r} \times \sum_{J=1}^{N_{\mathrm{P}}} \mathrm{e}^{\mathrm{i}\boldsymbol{q}\cdot\boldsymbol{R}_J},\end{aligned} \tag{9}$$

because the volumetric space occupied by the solvents is the total space V minus the volume occupied by the colloidal particles. The first term, being the Fourier transform of a constant, yields a contribution proportional to $\rho_{\mathrm{s}}\delta(q)$, where $\delta(\cdot)$ is the Dirac delta function and is appreciable only at $q = 0$. Therefore, this first term is excluded from further derivation.

Now, we combine the contributions from colloidal particles and the solvent, which leads to the following expression:

$$\begin{aligned}I_{\mathrm{coh}}(\boldsymbol{q}) &= \frac{1}{V}\left\langle \left| \int_{V_{\mathrm{p}}} \rho_{\mathrm{P}}(\boldsymbol{r}) \mathrm{e}^{\mathrm{i}\boldsymbol{q}\cdot\boldsymbol{r}} \mathrm{d}\boldsymbol{r} \times \sum_{J=1}^{N_{\mathrm{P}}} \mathrm{e}^{\mathrm{i}\boldsymbol{q}\cdot\boldsymbol{R}_J} \right.\right. \\ &\quad \left.\left. - \int_{V_{\mathrm{p}}} \rho_{\mathrm{S}} \mathrm{e}^{\mathrm{i}\boldsymbol{q}\cdot\boldsymbol{r}} \mathrm{d}\boldsymbol{r} \times \sum_{J=1}^{N_{\mathrm{P}}} \mathrm{e}^{\mathrm{i}\boldsymbol{q}\cdot\boldsymbol{R}_J} \right|^2 \right\rangle \\ &= \frac{1}{V}\left\langle \left| \int_{V_{\mathrm{p}}} \Delta\rho_{\mathrm{P}}(\boldsymbol{r}) \mathrm{e}^{\mathrm{i}\boldsymbol{q}\cdot\boldsymbol{r}} \mathrm{d}\boldsymbol{r} \times \sum_{J=1}^{N_{\mathrm{P}}} \mathrm{e}^{\mathrm{i}\boldsymbol{q}\cdot\boldsymbol{R}_J} \right|^2 \right\rangle,\end{aligned} \tag{10}$$

where $\Delta\rho_{\mathrm{P}}(\boldsymbol{r}) = \rho_{\mathrm{P}}(\boldsymbol{r}) - \rho_{\mathrm{s}}$ represents the excess scattering length density of the colloidal particle with respect to the solvent.

Next, we decompose the modulus as follows:

$$I_{\mathrm{coh}}(\boldsymbol{q}) = \frac{1}{V}\left\langle \int_{V_{\mathrm{p}}} \int_{V_{\mathrm{p}}} \Delta\rho_{\mathrm{P}}(\boldsymbol{r}) \Delta\rho_{\mathrm{P}}(\boldsymbol{r}') \mathrm{e}^{\mathrm{i}\boldsymbol{q}\cdot(\boldsymbol{r}-\boldsymbol{r}')} \mathrm{d}\boldsymbol{r}\, \mathrm{d}\boldsymbol{r}' \right.$$

$$\times \sum_{J=1}^{N_\mathrm{P}} \sum_{J'=1}^{N_\mathrm{P}} \mathrm{e}^{\mathrm{i}\boldsymbol{q}\cdot(\boldsymbol{R}_J-\boldsymbol{R}_{J'})} \Big\rangle. \tag{11}$$

It is further assumed that the ensemble averages of the first and second terms are statistically independent and can therefore be evaluated separately, as shown below:

$$I_\mathrm{coh}(\boldsymbol{q}) = \frac{1}{V}\left\langle \int_{V_\mathrm{p}}\int_{V_\mathrm{p}} \Delta\rho_\mathrm{P}(\boldsymbol{r})\Delta\rho_\mathrm{P}(\boldsymbol{r}')\,\mathrm{e}^{\mathrm{i}\boldsymbol{q}\cdot(\boldsymbol{r}-\boldsymbol{r}')}\,\mathrm{d}\boldsymbol{r}\,\mathrm{d}\boldsymbol{r}' \right\rangle \times\left\langle \sum_{J=1}^{N_\mathrm{P}} \sum_{J'=1}^{N_\mathrm{P}} \mathrm{e}^{\mathrm{i}\boldsymbol{q}\cdot(\boldsymbol{R}_J-\boldsymbol{R}_{J'})} \right\rangle. \tag{12}$$

This approximation relies on the assumption that neither the shape nor the scattering length density profile of the colloidal particle is correlated with the particle's center, which should be valid for spherically identical particles. Next, it can be defined that

$$F(\boldsymbol{q}) = \int_{V_\mathrm{p}} \Delta\rho_\mathrm{P}(\boldsymbol{r})\,\mathrm{e}^{\mathrm{i}\boldsymbol{q}\cdot\boldsymbol{r}}\,\mathrm{d}\boldsymbol{r}. \tag{13}$$

Evidently,

$$F(0) = \int_{V_\mathrm{p}} \Delta\rho_\mathrm{P}(\boldsymbol{r})\,\mathrm{d}\boldsymbol{r}. \tag{14}$$

Finally, with some straightforward reorganizations, the following expression is obtained:

$$I_\mathrm{coh}(\boldsymbol{q}) = n_\mathrm{P}F(0)^2\left\langle \frac{1}{F(0)^2}F(\boldsymbol{q})F^*(\boldsymbol{q}) \right\rangle \times\left\langle \frac{1}{N_\mathrm{P}}\sum_{J=1}^{N_\mathrm{P}} \sum_{J'=1}^{N_\mathrm{P}} \mathrm{e}^{\mathrm{i}\boldsymbol{q}\cdot(\boldsymbol{R}_J-\boldsymbol{R}_{J'})} \right\rangle, \tag{15}$$

where $n_\mathrm{P} = N_\mathrm{P}/V$ is the number density of the colloidal particles. Furthermore, the terms enclosed by the angular brackets are often defined as the form factor $P(\boldsymbol{q})$ and structure factor $S(\boldsymbol{q})$, which characterize the shape of a colloidal particle and positional correlations among particle centers, respectively. It is customary to normalize the form factor such that it decays from unity at $q = 0$, which explains the factor of $F(0)^2$. Thus, the coherent scattering intensity of spherically identical colloidal particles can be expressed as follows:

$$I_\mathrm{coh}(\boldsymbol{q}) = n_\mathrm{P}F(0)^2P(\boldsymbol{q})S(\boldsymbol{q}), \tag{16}$$

where

$$P(\boldsymbol{q}) = \left\langle \frac{1}{F(0)^2}F(\boldsymbol{q})F^*(\boldsymbol{q}) \right\rangle, \tag{17}$$

$$S(\boldsymbol{q}) = \left\langle \frac{1}{N_\mathrm{P}}\sum_{J=1}^{N_\mathrm{P}} \sum_{J'=1}^{N_\mathrm{P}} \mathrm{e}^{\mathrm{i}\boldsymbol{q}\cdot(\boldsymbol{R}_J-\boldsymbol{R}_{J'})} \right\rangle. \tag{18}$$

2.2. Colloids of monodisperse hard-sphere particles

The monodisperse hard-sphere colloidal particles can be considered spherically identical. Therefore, the derivation listed in Subsection 2.1 is applicable. Moreover, owing to their spherical symmetry, the resulting scattering intensity is expected to be isotropic. Consequently, the vector notation of the momentum transfer in both the form factor and structure factor expressions can be omitted. In addition, the interior of hard-sphere particles can be reasonably assumed to be compositionally homogeneous, allowing the scattering length density to be approximated as a constant. These characteristics of monodisperse hard-sphere colloids give rise to great simplifications in modeling the scattering intensity, as described below:

$$I_\mathrm{coh}(q) = n_\mathrm{P}\left(\Delta\rho_\mathrm{P}V_\mathrm{p}\right)^2P(q)S(q), \tag{19}$$

where

$$F(q) = \Delta\rho_\mathrm{P}\int_{V_\mathrm{p}} \mathrm{e}^{\mathrm{i}\boldsymbol{q}\cdot\boldsymbol{r}}\,\mathrm{d}\boldsymbol{r}, \tag{20}$$

$$F(0) = \Delta\rho_\mathrm{P}V_\mathrm{p}, \tag{21}$$

$$P(q) = \frac{1}{F(0)^2}\langle|F(q)|^2\rangle, \tag{22}$$

$$S(q) = \left\langle \frac{1}{N_\mathrm{P}}\sum_{J=1}^{N_\mathrm{P}} \sum_{J'=1}^{N_\mathrm{P}} \mathrm{e}^{\mathrm{i}\boldsymbol{q}\cdot(\boldsymbol{R}_J-\boldsymbol{R}_{J'})} \right\rangle. \tag{23}$$

We now focus on the form factor $P(q)$ by first deriving the explicit expression for $F(q)$. Let D denote the diameter of the hard-sphere particle; then,

$$\begin{aligned} F(q) &= \Delta\rho_\mathrm{P}\int_{V_\mathrm{p}} \mathrm{e}^{\mathrm{i}\boldsymbol{q}\cdot\boldsymbol{r}}\,\mathrm{d}\boldsymbol{r} \\ &= \Delta\rho_\mathrm{P}\int_0^{D/2} r^2\,\mathrm{d}r\int_0^{2\pi}\mathrm{d}\varphi\int_0^{\pi}\mathrm{e}^{\mathrm{i}qr\cos\theta}\sin\theta\,\mathrm{d}\theta \\ &= \frac{\Delta\rho_\mathrm{P}4\pi}{q^3}\left[\sin\left(\frac{qD}{2}\right)-\frac{qD}{2}\cos\left(\frac{qD}{2}\right)\right]. \end{aligned} \tag{24}$$

Note that $F(q)$ is real and isotropic, which is attributable to the spherical symmetry of the colloidal particles. Now, deriving the corresponding form factor of a homogeneous spherical particle with diameter D is straightforward, as shown below:

$$P(q) = \left\{24\left[\sin\left(\frac{qD}{2}\right)-\frac{qD\cos(qD/2)}{2}\right]\Big/(qD)^3\right\}^2. \tag{25}$$

The theoretical modeling of the structure factor $S(q)$ is based on liquid-state theory and is typically performed in real space rather than in reciprocal space. The structure factor $S(q)$ and the pair correlation function $g(r)$ form Fourier transform pairs. For isotropic systems, such as monodisperse hard-sphere colloids, the quantitative relationship between $S(q)$ and $g(r)$ can be expressed as follows:

$$S(q) = 1+4\pi n_\mathrm{p}\int_0^{\infty}[g(r)-1]\,r^2\frac{\sin(qr)}{qr}\,\mathrm{d}r. \tag{26}$$

Therefore, modeling $S(q)$ is equivalent to determining $g(r)$, for which we employ the Ornstein–Zernike (OZ) equation in the theory of simple liquids.[39] The physical interpretation of the OZ equation is intuitive: the total positional correlation between colloidal particles at two points is given by the sum

of their direct correlation and the indirect correlation mediated through all intermediate particles, as illustrated below:

$$h(r) = c(r) + n_{\mathrm{p}} \int c\left(\left|\boldsymbol{r} - \boldsymbol{r}'\right|\right) h\left(r'\right) \mathrm{d}\boldsymbol{r}', \tag{27}$$

where $c(r)$ denotes the direct correlation function and $h(r)$ represents the total correlation function. The integration term explicitly accounts for the contribution arising from indirect correlation mediated through a third point, namely, $\boldsymbol{r}'$. The total correlation function is related to the pair correlation function through the following expression:

$$h(r) = g(r) - 1. \tag{28}$$

The OZ equation is not closed and therefore requires an additional relation that connects the direct correlation function and total correlation function. In the literature, this additional relation is commonly introduced through an approximation known as a closure relation. Examples include Percus–Yevick (PY) closure, hypernetted chain (HNC) closure, Rogers–Young (RY) closure, and mean spherical approximation (MSA) closure. For monodispersed hard-sphere colloids, PY closure is commonly employed and is given as follows:

$$c(r) \approx \left\{1 - \exp\left[\frac{U(r)}{k_{\mathrm{B}}T}\right]\right\} g(r), \tag{29}$$

where k_{B} is the Boltzmann constant, T is the temperature, and $U(r)$ denotes the pairwise interaction potential. For hard-sphere colloids, the pair potential is defined as

$$U(r) = \begin{cases} \infty, & \text{for } \dfrac{r}{D} < 1, \\ 0, & \text{for } \dfrac{r}{D} \geq 1. \end{cases} \tag{30}$$

The structure factor resulting from the solution to the OZ equation coupled with PY closure for monodisperse hard-sphere colloids is given below:

$$S(q) = \frac{1}{1 - n_{\mathrm{p}} c(q)}, \tag{31}$$

$$c(q) = -\frac{4\pi}{q} \int_0^D \left(\alpha + \frac{\beta}{D} r + \frac{\delta}{D^3} r^3\right) \sin(qr)\, r\, \mathrm{d}r, \tag{32}$$

$$\alpha = \frac{(1+2\phi)^2}{(1-\phi)^4}, \tag{33}$$

$$\beta = -\frac{6\phi\,(1+0.5\phi)^2}{(1-\phi)^4}, \tag{34}$$

$$\delta = \frac{\phi\,(1+2\phi)^2}{2(1-\phi)^4}, \tag{35}$$

where ϕ is the volume fraction. The solution presented above is analytical and thus provides a great advantage for calculation.

2.3. Colloids of polydisperse hard-sphere particles

The following derivation is based on the work of Kotlarchyk and Chen[40] and begins with the following expression

$$I_{\mathrm{coh}}(\boldsymbol{q}) = \frac{1}{V} \left\langle \sum_{J=1}^{N_{\mathrm{P}}} \sum_{J'=1}^{N_{\mathrm{P}}} \left[\int_{V_J} \Delta\rho_J \, \mathrm{e}^{\mathrm{i}\boldsymbol{q}\cdot\boldsymbol{r}} \mathrm{d}\boldsymbol{r}\right] \times \left[\int_{V_{J'}} \Delta\rho_{J'} \, \mathrm{e}^{\mathrm{i}\boldsymbol{q}\cdot\boldsymbol{r}} \mathrm{d}\boldsymbol{r}'\right] \mathrm{e}^{\mathrm{i}\boldsymbol{q}\cdot(\boldsymbol{R}_J - \boldsymbol{R}_{J'})} \right\rangle. \tag{36}$$

V_J represents the volume occupied by the J-th colloidal particle, and $\Delta\rho_J$ represents the excess scattering length density. If all colloidal particles are identical, equation (36) reduces to Eq. (11). However, in polydisperse hard-sphere colloids, the diameters of the colloidal particles are not fixed but instead follow a continuous size distribution. As a result, the inner two integrals cannot be taken outside the summations. Similar to Eq. (13), it can be defined that

$$F_J(q) = \int_{V_J} \Delta\rho_J \, \mathrm{e}^{\mathrm{i}\boldsymbol{q}\cdot\boldsymbol{r}} \mathrm{d}\boldsymbol{r}, \tag{37}$$

where the integration is carried out over the volume occupied by the J-th colloidal particle. Substituting this into Eq. (37), the coherent scattering intensity becomes

$$I_{\mathrm{coh}}(\boldsymbol{q}) = \frac{1}{V} \left\langle \sum_{J=1}^{N_{\mathrm{P}}} \sum_{J'=1}^{N_{\mathrm{P}}} F_J(q) F_{J'}^*(q) \, \mathrm{e}^{\mathrm{i}\boldsymbol{q}\cdot(\boldsymbol{R}_J - \boldsymbol{R}_{J'})} \right\rangle. \tag{38}$$

Assuming that the particle size and orientation are statistically uncorrelated with the position of the particle center, which is generally valid for hard spherical colloids, then

$$I_{\mathrm{coh}}(\boldsymbol{q}) = \frac{1}{V} \left\langle \sum_{J=1}^{N_{\mathrm{P}}} \sum_{J'=1}^{N_{\mathrm{P}}} \langle F_J(q) F_{J'}^*(q) \rangle \, \mathrm{e}^{\mathrm{i}\boldsymbol{q}\cdot(\boldsymbol{R}_J - \boldsymbol{R}_{J'})} \right\rangle, \tag{39}$$

where the inner angular brackets denote averaging over particle size and orientation. According to Kotlarchyk and Chen,[40]

$$\langle F_J(q) F_{J'}^*(q) \rangle = [\langle |F(q)|^2 \rangle - |\langle F(q) \rangle|^2] \delta_{JJ'} + |\langle F(q) \rangle|^2, \tag{40}$$

where $\delta_{JJ'}$ is the Kronecker delta, which equals 1 when $J = J'$ and 0 otherwise. Plugging this result into the expression for the coherent scattering intensity, we obtain the following equation:

$$I_{\mathrm{coh}}(q) = n_{\mathrm{p}} \left[\langle |F(q)|^2 \rangle - |\langle F(q) \rangle|^2\right] + n_{\mathrm{P}} |\langle F(q) \rangle|^2 S(q). \tag{41}$$

Notably, the structure factor $S(q)$ in Eq. (41) is not strictly equivalent to its counterpart in Eq. (18), as the latter describes correlations among colloidal particles of identical size, whereas the former accounts for correlations in a polydisperse system where particle diameters vary continuously. To obtain a more concise formulation, the expression can be reorganized as follows:

$$I_{\mathrm{coh}}(q) = n_{\mathrm{p}} \langle |F(0)|^2 \rangle P(q) S'(q), \tag{42}$$

where

$$P(q) = \frac{\langle |F(q)|^2 \rangle}{\langle |F(0)|^2 \rangle}, \tag{43}$$

$$S'(q) = \{1 + \beta(q)[S(q) - 1]\}, \tag{44}$$

$$\beta(q) = \frac{|\langle F(q) \rangle|^2}{\langle |F(q)|^2 \rangle}. \tag{45}$$

To derive an explicit formulation for $P(q)$ and $\beta(q)$, one needs a statistical distribution of particle sizes. In the following, particulate radii are assumed to follow a Gaussian distribution. The probability density distribution function for the particle diameter is given by

$$f(D) = \frac{1}{\sqrt{2\pi}\sigma_D} \exp\left[-\frac{(D - \overline{D})^2}{2\sigma_D^2}\right], \tag{46}$$

where $\overline{D}$ and σ_D denote the mean and standard deviation of the Gaussian distribution, respectively. The scattering amplitude $F(q)$ for a homogenous sphere of diameter D is given by

$$F(q) = \frac{\Delta\rho_P 4\pi}{q^3}\left[\sin\left(\frac{qD}{2}\right) - \frac{qD}{2}\cos\left(\frac{qD}{2}\right)\right]. \tag{47}$$

Accordingly, the average form factor terms can be computed as follows:

$$\langle |F(q)|^2 \rangle = \int_0^\infty F(q)^2 f(D)\, \mathrm{d}D, \tag{48}$$

$$|\langle F(q) \rangle|^2 = \left[\int_0^\infty F(q) f(D)\, \mathrm{d}D\right]^2. \tag{49}$$

2.4. Smearing effect under pinhole geometry

An experimentally measured SANS spectrum is affected by smearing effects, which arise from uncertainties in determining the wavevector q. These uncertainties stem from the spread in the wavelength of incident neutrons, beam divergence, the finite spatial resolution of the detector, and other instrumental factors. To be more specific, under the pinhole geometry, the experimentally measured SANS spectrum denoted $I_{\mathrm{exp}}(q)$ is related to the ideal diffraction curve denoted $I_{\mathrm{coh}}(q)$ through the following convolution:

$$I_{\mathrm{exp}}(q) = \int I_{\mathrm{coh}}(q') R(q, q')\, \mathrm{d}q', \tag{50}$$

where $R(q, q')$ is the so-called resolution function, which is determined by the instrument design and measurement configuration. Note that equation (50) is not directly applicable to the small angle scattering spectra measured under slit geometry. Pederson *et al.* reported that the resolution function can be well approximated by a Gaussian function of the form[26]

$$R(q, q') = \frac{1}{\sqrt{2\pi}\sigma_q} \exp\left[-\frac{(q - q')^2}{2\sigma_q^2}\right], \tag{51}$$

where σ_q quantifies the uncertainty in q. In a standard scattering geometry, the wavevector is given by

$$q = \frac{4\pi \sin\theta}{\lambda}, \tag{52}$$

where λ is the wavelength and θ is half of the scattering angle. It is understandable that both the uncertainties in the scattering angle and in the wavelength of incident neutrons contribute to total uncertainty in q. Assuming both factors are independent, then one can apply the rule of error propagation as follows:

$$(\mathrm{d}q)^2 = \left(\frac{\partial q}{\partial \theta}\right)^2 (\mathrm{d}\theta)^2 + \left(\frac{\partial q}{\partial \lambda}\right)^2 (\mathrm{d}\lambda)^2, \tag{53}$$

where

$$\left(\frac{\partial q}{\partial \theta}\right)^2 = \left(\frac{4\pi\cos\theta}{\lambda}\right)^2 = \left(\frac{4\pi}{\lambda}\right)^2 (1 - \sin^2\theta) = \left[\left(\frac{4\pi}{\lambda}\right)^2 - q^2\right], \tag{54}$$

$$\left(\frac{\partial q}{\partial \lambda}\right)^2 = \left(\frac{4\pi\sin\theta}{\lambda}\right)^2 \left(\frac{1}{\lambda}\right)^2 = q^2 \left(\frac{1}{\lambda}\right)^2. \tag{55}$$

Hence, one gets the following expression:

$$(\mathrm{d}q)^2 = \left[\left(\frac{4\pi}{\lambda}\right)^2 - q^2\right](\mathrm{d}\theta)^2 + q^2\left(\frac{1}{\lambda}\right)^2 (\mathrm{d}\lambda)^2. \tag{56}$$

Next, we perform statistical averaging on both sides of the equation and it leads to the equation below:

$$\sigma_q^2 = \left[\left(\frac{4\pi}{\lambda}\right)^2 - q^2\right]\sigma_\theta^2 + q^2\left(\frac{1}{\lambda}\right)^2 \sigma_\lambda^2, \tag{57}$$

where σ_q, σ_θ, and σ_λ are the standard deviations of q, θ, and λ, respectively. When a mechanical velocity selector is applied to monochromatize the neutron beam in a reactor-based SANS spectrometer, it is found that the wavelengths of the monochromatized neutrons often follow a triangular distribution; hence, the full-width-at-half-maximum (FWHM) (denoted Δ_λ) is commonly employed instead. As such, the standard deviation of q can be expressed as follows:

$$\sigma_q^2 = \left[\left(\frac{4\pi}{\lambda}\right)^2 - q^2\right]\sigma_\theta^2 + q^2\left(\frac{1}{2\sqrt{2\ln 2}}\frac{\Delta_\lambda}{\lambda}\right)^2. \tag{58}$$

Note that σ_q^2 can be more explicitly modelled based on the parameters including sample to detector distance, dimensions of detector pixels, radius of source aperture, etc. for the conventional pinhole geometry and SANS equipped with reflecting mirror or focusing lenses. However, that is beyond the scope of the present paper.

3. Results and discussion

On the basis of the equations presented above, we performed a theoretical synthesis of SANS spectra for both

monodisperse and polydisperse hard-sphere colloidal systems. The wavevector range 0.001–0.5 Å^{-1} was selected to reflect the standard measurement range accessible by typical SANS instruments.

3.1. Scattering curves of monodisperse hard-sphere colloids

Figure 1 shows the form factor $P(q)$ of monodisperse hard-sphere colloids whose diameters range from 30 Å to 3000 Å. In panel (a), the curves are plotted in the form of $P(q)$ versus q. At $D = 30$ Å, the magnitude of $P(q)$ remains close to unity from low-q up to $q = 0.1$ Å^{-1}, followed by a sharp decrease in q. With increasing diameter, the curves gradually shift to the left while keeping the overall shape unchanged. As a result, the range of q values over which $P(q)$ remains appreciable becomes progressively narrower. In Panel (b), the curves are replotted in the form of $P(q)$ versus $q \times D$. All the curves collapse onto a single master curve, which suggests that the shape of the monodisperse hard-sphere colloid is fixed, whereas its relative position in q-space is determined by the diameter D. Moreover, the magnitude of the oscillation decays following a power-law behavior with an exponent of -4.

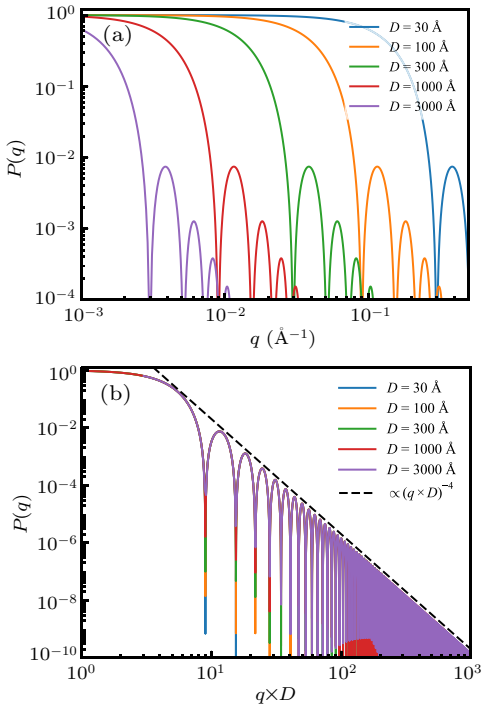


Fig. 1. Form factors of monodisperse hard-sphere colloids with various particle diameters. In panel (a), the curves are plotted as $P(q)$ versus q; in panel (b), the curves are plotted as $P(q)$ versus $q \times D$. See the legends for the color code of the particle diameters.

Figure 2 shows the structure factors $S(q)$ of monodisperse hard-sphere colloids with different particle diameters at volume fractions ranging from 0.01 to 0.4. In panel (a), the diameter is set to 30 Å. At the lowest volume fraction of 0.01, the curve is almost featureless, showing a nearly flat profile close to unity across the q range accessible by SANS. Upon increasing the volume fraction ϕ from 0.05 to 0.4, a strong interaction peak gradually develops at approximately $q = 0.2$ Å^{-1}. Panels (b) and (c) show the results for particle diameters of 300 Å and 3000 Å, respectively. While the general trend remains consistent with that in panel (a), a clear shift in the interaction peak toward lower q values is observed at higher volume fractions. In panel (d), all the structure factor curves are replotted as a function of the dimensionless variable $q \times D$, which is similar to the representation employed in Fig. 1(b). The collapse of the curves onto a single master curve confirms that the shape of $S(q)$ is primarily determined by the volume fraction ϕ, whereas the particle diameter D scales the particle position in q-space.

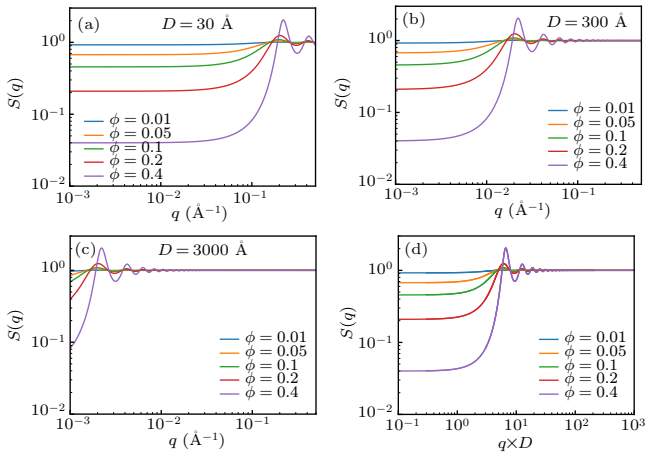


Fig. 2. Structure factors of monodisperse hard-sphere colloids with various particle diameters and volume fractions: (a) $D = 30$ Å, (b) $D = 300$ Å, (c) $D = 3000$ Å, and (d) structure factors plotted against $q \times D$, showing collapse of the curves for different diameters. See the legends for the color code of the volume fractions.

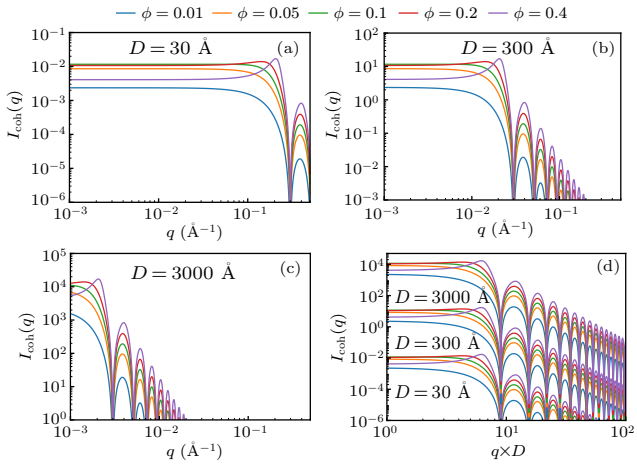


Fig. 3. Theoretical diffraction curves showing the coherent scattering intensity of monodisperse colloids with various particle diameters and volume fractions. Panel (a) $D = 30$ Å; panel (b) $D = 300$ Å; panel (c) $D = 3000$ Å; and panel (d) coherent scattering intensities plotted against $q \times D$. See the legends for the color code of the volume fractions. Note that the unit of the vertical axis is cm^{-1}.

To synthesize the theoretical diffraction curves, a scattering contrast is needed. In this study, it is assumed to be

$\Delta\rho_P = 4.25 \times 10^{-7}$ Å^{-2}. The volume fraction can be calculated as the product of the number density and the volume of an individual particle, i.e., $\phi = n_p \times V_p$. The calculation results are shown in Fig. 3. In panel (a), the particle diameter is set to 30 Å. In the low-q regime up to $q = 0.1$ Å^{-1}, the scattering intensity is almost independent of q; however, the corresponding magnitudes show a nonmonotonic dependence on the volume fraction. This behavior arises from the competing effects of the structure factor and the intensity prefactor: while the low-q limit of the structure factor related to isothermal compressibility decreases with increasing volume fraction, the intensity prefactor is proportional to the volume fraction. At $q \sim 0.2$ Å^{-1}, an interaction peak emerges, reflecting the underlying structure factor. At even higher q values, the strong oscillation is apparently inherited from the form factor. Panels (b) and (c) correspond to particle diameters of 300 Å and 3000 Å, respectively. The overall shapes of each curve remain nearly unchanged across different volume fractions, whereas their relative positions shift toward lower q values and higher magnitudes with increasing volume fraction. In panel (d), the scattering curves are replotted against $q \times D$. In this representation, the scattering curves belonging to the same volume fraction collapse onto a single profile in terms of both shape and position, whereas differences in magnitude are attributed to differences in volume fraction.

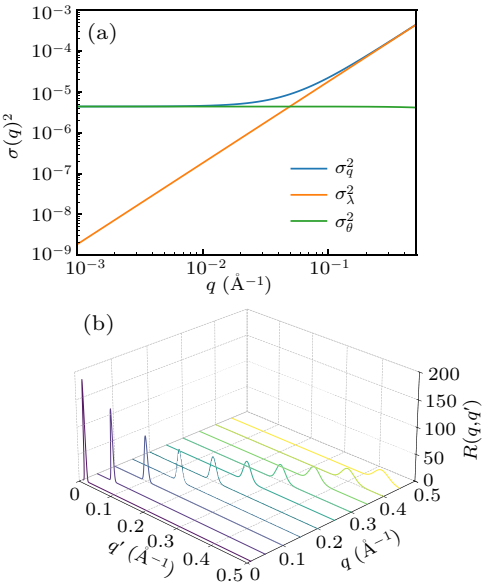


Fig. 4. Characteristics of the resolution function. Panel (a) total standard deviation of q along with the individual contributions arising from the spread in wavelength of incident neutrons (denoted σ_λ) and the scattering angle (denoted σ_θ). Panel (b) Resolution function $R(q,q')$ plotted with q' on the x-axis and q on the y-axis. The units of the vertical axes for panels (a) and (b) are Å^{-2} and Å, respectively.

To calculate the resolution function, it is assumed that the relative wavelength spread $\Delta_\lambda/\lambda = 10\%$, the mean wavelength $\lambda = 6$ Å, and the angular uncertainty of $\sigma_\theta = 10^{-3}$, which reflects the typical setup for SANS measurements. The resulting standard deviation of q, denoted σ_q, is illustrated in Fig. 4. Panel (a) illustrates the total σ_q as well as the separate contributions from the wavelength spread and scattering angle. In the low-q regime up to $q \sim 0.01$ Å^{-1}, the dominant contribution arises from the wavelength spread, yielding an almost constant σ_q. As q increases, the effect related to the scattering angle becomes more pronounced, resulting in a gradual increase in the total $\sigma(q)$. Panel (b) displays the corresponding resolution function $R(q,q')$ at selected values of q.

Figure 5 shows the ideal diffraction curves from Fig. 3 after smearing by the resolution function shown in Fig. 4. The panel layout and color coding of the curves are the same as those in Fig. 3. The characteristic features of the scattering curves become less pronounced upon incorporating the smearing effect. In particular, the depth of the minima separating the oscillations at high q values, originating from the form factor, becomes significantly shallower. Moreover, the smearing effect is more evident for colloids with large particle diameters, as shown in panel (c), than for those with smaller diameters, as shown in panel (a); this trend is clearly observed in panel (d).

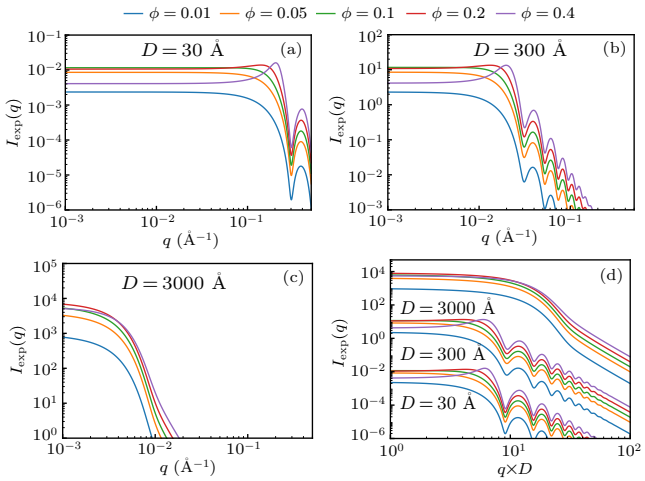


Fig. 5. Synthesized SANS spectra modeling the experimentally measured coherent scattering intensity for monodisperse colloids with various particle diameters and volume fractions. The panel arrangement and color coding of the curves are the same as those in Fig. 3. The unit of the vertical axis is cm^{-1}.

3.2. Scattering curves of polydisperse hard-sphere colloids

Figure 6 presents the form factors $P(q)$ of polydisperse hard-sphere colloids, assuming Gaussian distributions for particle radii. Panels (a), (b), and (c) correspond to mean particle diameters of 30 Å, 300 Å, and 3000 Å, respectively. The degree of polydispersity is quantified by the index $\xi = \sigma_D/\bar{D}$, and different values of ξ are illustrated in distinct colors. In particular, $\xi = 0$ is equivalent to the case of monodisperse particles. The $P(q)$ curves exhibit a systematic shift toward lower q values with increasing particle radius while retaining their overall shape. Furthermore, in comparison with those in the monodisperse case, the oscillatory features of the form fac-

tor progressively diminish and eventually vanish with increasing polydispersity index. For example, in panel (a), as the polydispersity index ξ increases from 0 to 0.1, the peak centered at approximately 0.3 Å^{-1} shifts noticeably to a lower q; when ξ reaches 0.2, the peak becomes indistinguishable, and at an ξ of 0.4, this characteristic feature nearly disappears. Similar trends are observed in panels (b) and (c), corresponding to larger particle diameters. In panel (d), all curves are plotted against $q \times \bar{D}$ resulting in collapse into a single curve. This confirms that the shape of the spectra for the polydisperse hard-sphere colloid remains consistent across different particle sizes, whereas its relative position in q-space is determined by the diameter D, which is consistent with the behavior observed in the monodisperse case. These observations reveal that the introduction of polydispersity substantially modifies the form factor profile, thereby increasing the complexity in analyzing the structural properties of such samples.

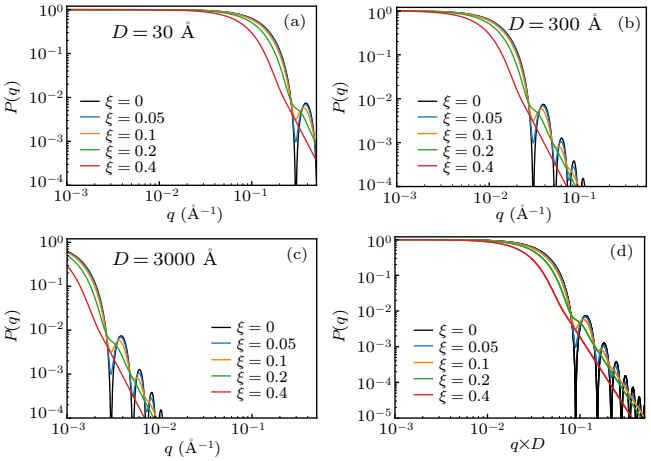


Fig. 6. Form factors of polydisperse hard-sphere colloids with different particle sizes and degrees of polydispersity. Panels (a), (b), and (c) correspond to mean particle diameters of 30 Å, 300 Å, and 3000 Å, respectively, with the curves plotted as $P(q)$ versus q. Panel (d) shows the same data plotted as $P(q)$ versus $q \times \bar{D}$. Polydispersity is indicated by the color code shown in the legend.

Figure 7 presents the form of $\beta(q)$ in panel (a) and the apparent structure factors $S'(q)$ for polydisperse hard-sphere colloids at volume fractions of 0.1, 0.2, and 0.4, as shown in panels (b), (c), and (d), respectively. The polydispersity index ξ ranges from 0 to 0.4 and is represented by distinct colors. All curves are plotted against $q \times \bar{D}$. In panel (a), $\beta(q)$ equals unity when $\xi = 0$, corresponding to the monodisperse case. For nonzero ξ, $\beta(q)$ oscillates between 0 and 1. As the polydispersity index increases, the overall magnitude of $\beta(q)$, especially at high q, decreases. The apparent structure factors $S'(q)$ exhibit complex evolution with increasing polydispersity. In all three volume fraction cases, the low-q limit gradually increases. The first primary peak, located at approximately $q \times \bar{D} \approx 5$, diminishes in intensity and shifts toward a lower q. Moreover, secondary peaks emerge near $q \times \bar{D} \approx 8$ and 16, but these features eventually fade as the polydispersity index increases.

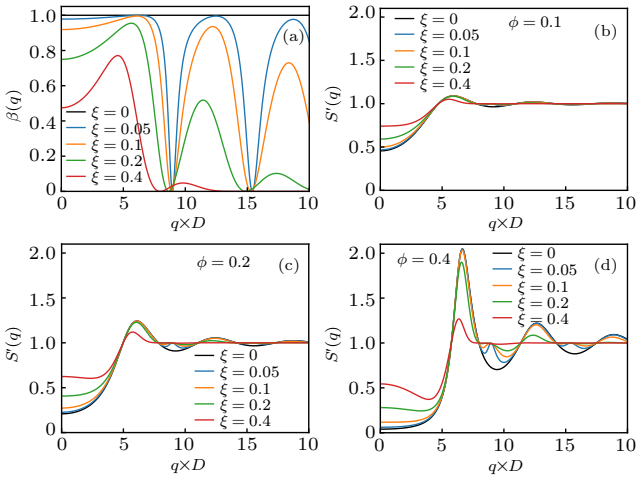


Fig. 7. Panel (a) shows the $\beta(q)$ function, while panels (b), (c), and (d) present the apparent structure factor $S'(q)$ for polydisperse hardsphere colloids at selected volume fractions of 0.1, 0.2, and 0.4, respectively. See Section 2 for their definitions. Different colors represent different polydispersity indices. All curves are plotted against $q \times \bar{D}$.

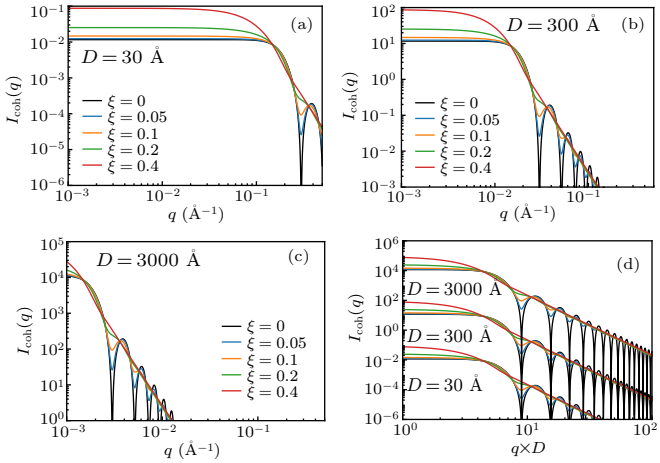


Fig. 8. Theoretically synthesized diffraction curves for polydisperse hard colloids at a volume fraction of 0.1 and various mean particle radii. Panel (a) $D = 30$ Å, panel (b) $D = 300$ Å, panel (c) $D = 3000$ Å, and panel (d) all results plotted against $q \times D$. The color codes representing different polydispersity indices are provided in the legend. The unit of the vertical axis is cm^{-1}.

Figure 8 presents the theoretically synthesized diffraction curves for polydisperse hard sphere colloids at a volume fraction of 0.1 and different mean particle radii. Panels (a), (b), and (c) correspond to mean particle radii of 30 Å, 300 Å, and 3000 Å, respectively. The polydispersity index ranges from 0 to 0.4. Two discernible effects of increasing the polydispersity are observed. First, the intensity at low q increases. This is attributed to the enhanced contribution from large particles in the polydispersity distribution, which dominates the low-q scattering. Second, the characteristic oscillations at high q, reminiscent of the form factor of a spherical particle, gradually diminish and eventually disappear. This attenuation arises because the oscillations associated with the form factors of spheres with different radii are out of phase, leading to their

mutual cancellations. Hence, the broader the size distribution is, the more complete this destructive interference becomes. In panel (d), all curves are plotted versus $q \times \bar{D}$. Increasing the particle radius shifts the curves upward in intensity but does not alter their overall shape.

Figure 9 shows the theoretically synthesized SANS spectra for polydisperse hard-sphere colloids at a volume fraction of 0.1, considering the smearing effect. Panels (a), (b), and (c) correspond to mean particle radii of 30 Å, 300 Å, and 3000 Å, respectively. The polydispersity index ranged from 0 to 0.4. The smearing effect further suppresses the oscillatory features of the spectra at high q values. This suppression is more pronounced for colloids with larger mean particle radii, as shown in panel (d), where all the curves are plotted together for comparison. This observation is consistent with the observation shown in Fig. 5 for monodisperse hardsphere colloids.

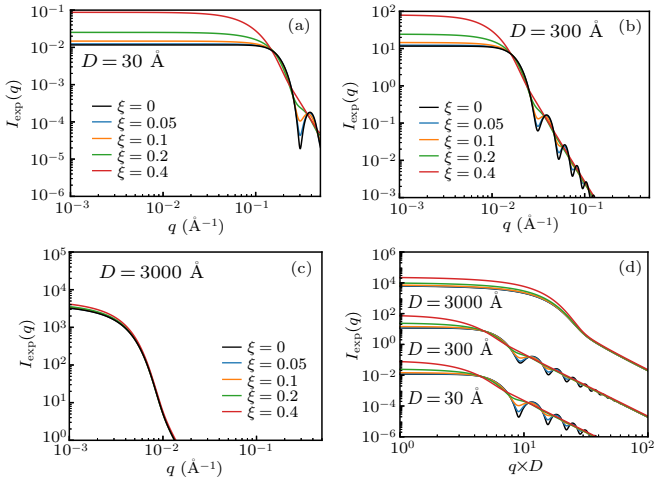


Fig. 9. Theoretically synthesized SANS spectra for polydisperse hardsphere colloids at a volume fraction of 0.1, with the smearing effect being considered. The panel arrangement and color code are the same as those in Fig. 8. The unit of the vertical axis is cm^{-1}.

4. Conclusions

Small angle scattering is a power technique and there are ongoing tremendous efforts devoted to facilitating this technique.[41,42] In this paper, we present a theoretical framework that allows for the theoretical synthesis of SANS spectra of monodisperse and polydisperse hard-sphere colloids and that incorporates the smearing effect that arises from various experimental limitations, such as the finite wavelength spread and the large beam footprint of incident neutrons. Within this framework, the adjustable parameters include the particle diameter, polydispersity index, and volume fraction for characterizing the colloidal system, as well as the neutron wavelength, its relative spread, and the uncertainty of scattering angle for describing the measurement setup.

The results indicate that the smearing effect can considerably undermine the characteristic features in the diffraction curves that reflect the microstructural signatures of hardsphere colloids. In particular, the impact of smearing is more pronounced for systems with larger particle radii. On the basis of this framework, we developed in-house Python codes to generate an SANS spectral dataset consisting of matched triplets: the ideal diffraction curve, the resolution function, and the corresponding smeared spectrum. Building on this foundation, we are currently developing a machine learning-based de-smearing protocol, the results of which will be reported in future publications.

Acknowledgements

Bin Wu would like to acknowledge the funding supports by the Large Scientific Facility Open Subject of Songshan Lake, Dongguan, Guangdong (Grant No. KFKT2022B12) and the National Natural Science Foundation of China (Grant No. 12375294). Takuya Iwashita is supported by Grant-in-Aid for Transformative Research Areas (B), "Rheology of Disordered Structures: Establishing Anankeon Dynamics", JSPS KAKENHI (Grant Nos. 22B206 and 22H05040), and by Oita University President's Strategic Discretionary Fund.

References

[1] Penttilä P A, Altgen M, Awais M, Österberg M, Rautkari L and Schweins R 2020 *Sci. Rep.* **10** 20844
[2] Pan Q, Zhang L, Feng R, Lu Q, An K, Chuang A C, Poplawsky J D, Liaw P K and Lu L 2021 *Science* **374** 984
[3] Lopez C G, Watanabe T, Martel A, Porcar L and Cabral J T 2015 *Sci. Rep.* **5** 7727
[4] Zákutná D, Graef K, Dresen D, Porcar L, Honecker D and Disch S 2021 *Colloid Polym. Sci.* **299** 281
[5] Shibata M, Nakanishi Y, Abe J, Arima-Osonoi H, Iwase H, Shibayama M, Motokawa R, Kumada T, Takata S, Yamamoto K, Takenaka M and Miyazaki T 2023 *Polym. J.* **55** 1165
[6] Shrestha U R, Mamontov E, O'Neill H M, Zhang Q, Kolesnikov A I and Chu X 2022 *Innovation* **3** 100199
[7] Longo M, Heigl R J and Schrader T E 2021 *J. Cryst. Growth* **576** 126362
[8] Ramsay J and Lindner P 1993 *J. Chem. Soc.-Faraday Trans.* **89** 4207
[9] Orts W J, Godbout L, Marchessault R H and Revol J F 1998 *Macromolecules* **31** 5717
[10] Cherhal F, Cousin F and Capron I 2015 *Langmuir* **31** 5596
[11] Trewhella J 2022 *Structure* **30** 15
[12] Hayward D W, Chiappisi L, Prévost S, Schweins R and Gradzielski M 2018 *Sci. Rep.* **8** 7299
[13] Yamamoto A, Higaki Y, Thoma J, Kimmle E, Ishige R, Demé B, Takahara A and Tanaka M 2022 *Polym. J.* **54** 57
[14] Wu B, Li X, Do C, Kim T H, Shew C Y, Liu Y, Yang J, Hong K, Porcar L, Chen C Y, Liu E L, Smith G S, Herwig K W and Chen W R 2011 *J. Chem. Phys.* **135** 144903
[15] Stieger M, Richtering W, Pedersen J S and Lindner P 2004 *J. Chem. Phys.* **120** 6197
[16] Stieger M, Pedersen J S, Lindner P and Richtering W 2004 *Langmuir* **20** 7283
[17] Pedersen J S, Svaneborg C, Almdal K, Hamley I W and Young R N 2003 *Macromolecules* **36** 416
[18] Yurekli K, Mitchell C A and Krishnamoorti R 2004 *J. Am. Chem. Soc.* **126** 9902
[19] Rafique A S, Khodaparast S, Poulos A S, Sharratt W N, Robles E S J and Cabral J T 2020 *Soft Matter* **16** 7835
[20] Li N, Li X, Wang Y, Liu G, Zhou P, Wu H, Hong C, Bian F and Zhang R 2016 *J. Appl. Crystallogr.* **49** 1428

[21] Xu J, Xia Y, Li Z, Chen H, Wang X, Sun Z and Yin W 2021 *Nucl. Instrum. Method A* **1013** 165642

[22] Wignall G D, Christen D K and Ramakrishnan V 1988 *J. Appl. Crystallogr.* **21** 438

[23] Wignall G D 1991 *J. Appl. Crystallogr.* **24** 479

[24] Barker J G and Pedersen J 1995 *J. Appl. Crystallogr.* **28** 105

[25] Pedersen J S 1993 *Resolution effects and analysis of small-angle neutron scattering data. Le Journal de Physique IV* 3

[26] Pedersen J S, Posselt D and Mortensen K 1990 *J. Appl. Crystallogr.* **23** 321

[27] Glatter O 1974 *J. Appl. Crystallogr.* **7** 147

[28] Glatter O 1977 *J. Appl. Crystallogr.* **10** 415

[29] Hould N, Lobo R and Wagner N 2010 *Part. Part. Syst. Char.* **27** 89

[30] Linder P and Zemb Th 2002 *Neutrons, X-rays and Light: Scattering Methods Applied to Soft Condensed Matter* (Amsterdam: North Holland)

[31] Lake J A 1967 *Acta Crystallogr.* **23** 191

[32] van Cittert P H 1930 *Z. Physik* **65** 547

[33] Vad T and Sager W F C 2011 *J. Appl. Cryst.* **44** 32

[34] Huang G R, Tung C H, Chen M Z, Porcar L, Shinohara Y, Wildgruber C, Do C and Chen W R 2023 *J. Appl. Crystallogr.* **56** 1537

[35] Tung C H, Hsiao Y J, Chen H L, Huang G R, Porcar L, Chang M C, Carrillo J M, Wang Y, Sumpter B G, Shinohara Y, Taylor J, Do C and Chen W R 2024 *J. Colloid Interf. Sci.* **659** 739

[36] Song G, Porcar L, Boehm M, Cecillon F, Dewhurst C, Goc Y L, Locatelli J, Mutti P and Weber T 2020 *EPJ Web Conf.* **225** 01004

[37] Chang M C, Wei Y, Chen W R and Do C 2020 *MRS Commun.* **10** 11

[38] Chen S H 1986 *Annu. Rev. Phys. Chem.* **37** 351

[39] Hansen J P and McDonald I R 2006 *Theory of Simple Liquids* (3rd edn.) (New York: Academic Press)

[40] Kotlarchyk M and Chen S 1983 *J. Chem. Phys.* **79** 2461

[41] Wang J, Liu J, Xu D, Grünauer F, Hao L, Liu Y, Zhang H, Cheng P and Bao W 2024 *Chin. Phys. B* **33** 057801

[42] Xie F, Xie M, Song B, Guo Q and Jiao X 2024 *Chin. Phys. B* **33** 120101